PRL 118, 086101 (2017) PHYSICAL REVIEW LETTERS 24 FEBRUARY 2017

Quantitative Agreement between Electron-Optical Phase Images of WSe_2 and Simulations Based on Electrostatic Potentials that Include Bonding Effects

S. Borghardt,[1,*] F. Winkler,[2,3] Z. Zanolli,[4,5] M. J. Verstraete,[6] J. Barthel,[2,7] A. H. Tavabi,[2,3]
R. E. Dunin-Borkowski,[2,3] and B. E. Kardynał[1]
[1]*Peter Grünberg Institute 9 (PGI-9), Forschungszentrum Jülich, D-52425 Jülich, Germany*
[2]*Ernst Ruska-Centre for Microscopy and Spectroscopy with Electrons (ER-C), Forschungszentrum Jülich, D-52425 Jülich, Germany*
[3]*Peter Grünberg Institute 5 (PGI-5), Forschungszentrum Jülich, D-52425 Jülich, Germany*
[4]*Peter Grünberg Institute 1 (PGI-1) and Institute for Advanced Simulations (IAS-1), Forschungszentrum Jülich, D-52425 Jülich, Germany*
[5]*Institute for Theoretical Solid State Physics and European Theoretical Spectroscopy Facility, RWTH Aachen University, D-52056 Aachen, Germany*
[6]*NanoMat / Q-Mat / CESAM and European Theoretical Spectroscopy Facility, Université de Liège (B5), B-4000 Liège, Belgium*
[7]*Gemeinschaftslabor für Elektronenmikroskopie (GFE), RWTH Aachen University, D-52074 Aachen, Germany*

(Received 7 October 2016; revised manuscript received 13 December 2016; published 22 February 2017)

The quantitative analysis of electron-optical phase images recorded using off-axis electron holography often relies on the use of computer simulations of electron propagation through a sample. However, simulations that make use of the independent atom approximation are known to overestimate experimental phase shifts by approximately 10%, as they neglect bonding effects. Here, we compare experimental and simulated phase images for few-layer WSe_2. We show that a combination of pseudopotentials and all-electron density functional theory calculations can be used to obtain accurate mean electron phases, as well as improved atomic-resolution spatial distribution of the electron phase. The comparison demonstrates a perfect contrast match between experimental and simulated atomic-resolution phase images for a sample of precisely known thickness. The low computational cost of this approach makes it suitable for the analysis of large electronic systems, including defects, substitutional atoms, and material interfaces.

DOI: 10.1103/PhysRevLett.118.086101

The complex wave function of electrons that have passed through a sample in the transmission electron microscope (TEM) can be reconstructed using the technique of off-axis electron holography. For a nonmagnetic sample, the phase of the electron wave function is related to the three-dimensional electrostatic potential in the specimen and, in the absence of dynamical scattering, is proportional to the integral of the electrostatic potential in the electron beam direction [1]. As a result of the high spatial resolution of the TEM, off-axis electron holography is therefore a powerful technique for the characterization of local variations in electrostatic potential in functional materials at the nanoscale [2].

In general, the conversion of a recorded phase image into a potential is nontrivial and often has to be supported by atomistic computer simulations [3]. An approach that is used frequently makes use of the independent atom approximation (IAA) and involves representing the crystal potential as a superposition of electrostatic potentials of individual isolated atoms [4]. As the effects of bonding are neglected, the results of simulations based on this approximation overestimate the mean phase of the electron wave function when compared to experimental measurements [5]. The accuracy of calculated mean electron phases has been shown to improve when using density functional theory (DFT) for the calculation of electrostatic potentials to take bonding effects into account [6,7]. However, to the best of our knowledge, no comparison between the DFT-calculated atomic-resolution spatial distribution of the electron phase and high-resolution electron holography experiments has been performed. The importance of developing a technique suitable for such comparisons is growing, as the operation of modern electronic and optoelectronic devices relies more frequently on or is affected by individual atoms and local structure variations [8,9]. The identification and characterization of such defects are, hence, of great importance for the understanding and further improvement of the performance of both current and future optoelectronic devices. This requirement applies especially to the emerging field of two-dimensional materials, where, due to their very limited thickness, the manipulation of individual atoms strongly affects the properties of the materials.

In addition to the approximations that are used in simulations, experimental uncertainties often prevent quantitative comparisons with measurements. The most common experimental uncertainties include a poor knowledge of the sample thickness, which can be difficult to determine with sufficient precision at high spatial resolution, as well as the possible presence of crystal defects, surface damage, reconstructions, and contamination [10]. In this regard, transition metal dichalcogenides (TMDs), which have the chemical composition MX_2, where M and X denote a transition metal and a chalcogen, respectively, are an exception. They are layered materials that can be prepared with a thickness of an integer number of monolayers and do not form surface dangling bonds, which are responsible for surface reconstructions in other materials. Although surface contamination still presents a major problem for off-axis electron holography of TMDs, clean areas can often be identified and studied [11].

The possibility of reconstructing the true crystal potentials of TMDs using off-axis electron holography is highly attractive, because they provide a model system that allows the phase evolution of electrons passing through thin samples to be understood. Additionally, they are promising for optoelectronic devices, including transistors, light sources, and photodetectors [12–14]. Their properties can be tuned by fabricating heterostructures [15–17] and by defect engineering [18,19].

Here, we show that both the mean phase of few-layer TMDs measured using off-axis electron holography and the atomic-scale spatial redistribution of the phase can be described accurately using simulations based on three-dimensional potentials that include the effects of bonding. In order to demonstrate these benefits, we compare average electron phases obtained using both DFT and IAA calculations and their spatial distributions with our experimental results [11]. The effects of bonding are assessed by comparing crystal potentials obtained from calculations that include bonding effects with ones that neglect them.

In this work, pseudopotential and all-electron DFT calculations were performed using the ABINIT and Elk software packages, respectively [20–22]. A detailed description of the calculations and an overview of the computation parameters can be found in the Supplemental Material [23].

As a preliminary step for the calculation of electrostatic potentials, relaxation calculations were carried out in order to obtain the crystal structure of WSe_2 (Fig. 1) for thicknesses of up to five layers.

The use of plane wave basis sets and pseudopotentials reduces the number of active electrons and the kinetic energy cutoff. This is common practice and provides access to the large system sizes that are needed for defects and heterostructures. However, it does not explicitly give the core electron charge, which is frozen out of the pseudopotential but is needed for TEM simulations. In order to access the full electrostatic potential from DFT calculations, we apply a correction scheme, as reported in Ref. [27] and explained in detail in the Supplemental Material [23].

Two different methods that both neglect the effects of bonding were compared with the DFT results. First, crystal potentials were determined by the IAA method using elastic electron scattering factors from the literature [28].

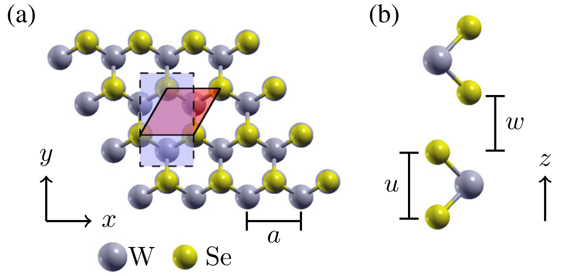

FIG. 1. WSe_2 lattice geometry. (a) Top view with the red rhombus marking the unit cell used in DFT calculations and the blue rectangle marking the cell used in multislice simulations of electron-optical phase images. (b) Side view of a unit cell, which comprises a stack of two monolayers.

Second, independent DFT (IDFT) calculations were used to obtain the electrostatic potentials for crystals of independent atoms. One purpose of using the IDFT method was to determine the change in spatial electron density resulting from bonding effects by evaluating the difference between spatial electron densities obtained by the IDFT and DFT methods. The second purpose of using the IDFT method was to rule out numerical artifacts as the reason for any differences between the DFT and IAA calculations by matching the numerical parameters used for the DFT and IDFT methods.

In order to compare spatially averaged electrostatic potentials obtained using the three different methods, they were averaged within the x-y plane, integrated in the z direction and normalized to the number of layers N, according to the expression

$$V_{\mathrm{int}} = \frac{1}{N}\frac{\int V(x,y,z)dxdydz}{\int dxdy}.$$

The integrated plane-averaged potential V_{int} can be related approximately to the more commonly used mean inner potential V_0 by dividing V_{int} by the bulk layer periodicity, which is not defined for few-layer systems. Figure 2 shows both V_{int} and V_0 plotted against the number of layers. The results obtained using all three methods are found to be independent of the number of layers, as a result of the weak interlayer interactions and the absence of surface effects. Furthermore, the DFT method yields the lowest potentials, whereas the IAA and IDFT results exceed the DFT values by approximately 9% and 6%, respectively. The difference between the IDFT and IAA values can be explained by the use of a different computational technique: the scattering factors that were used as input for IAA electrostatic potentials were obtained from relativistic Hartree-Fock calculations [7].

In order to relate differences between the DFT and IDFT calculations to a spatial change in electron density associated with bonding, differences between both the spatial electron densities and the electrostatic potentials were

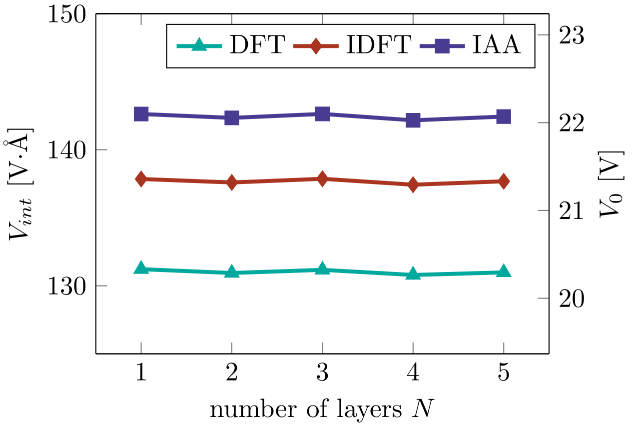

FIG. 2. Integrated plane-averaged electrostatic potential per layer (left axis) and mean inner potential (right axis) for few-layer WSe_2 calculated using three different methods.

calculated for a WSe_2 monolayer, as shown in Fig. 3. In comparison to IDFT, DFT shows a higher electron density in the interstitial regions of the crystal and a correspondingly lower electron density in the proximity of the nuclei. This shift in electron density is to be expected for covalent bonding between W and Se atoms. As a consequence of this shift, the electrostatic potential is decreased along the bonding directions close to the Se nuclei and within the Se columns.

Figure 3 shows that the relationship between n and V is nonlinear, with a small shift in electron density leading to a significant decrease in electrostatic potential. The minimum and maximum differences between the DFT and IDFT electron densities are $-0.023n_0$ and $0.026n_0$, respectively, while the minimum and maximum differences between the electrostatic potentials are $-0.142V_0$ and $0.003V_0$, respectively. Here, n_0 and V_0 are the bulk average electron density and the bulk mean inner potential of WSe_2, respectively [29]. Positive values denote higher electron densities and higher potentials in the DFT method.

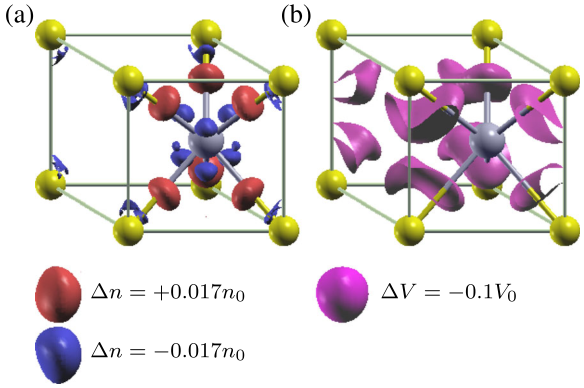

FIG. 3. (a) Change in spatial electron density and (b) change in electrostatic potential in a WSe_2 monolayer unit cell between the DFT and IDFT methods with n_0 and V_0 the bulk average electron density and the bulk mean inner potential of WSe_2, respectively [29]. Negative values denote lower electron densities and lower electrostatic potentials in the DFT method.

Electrostatic potentials simulated using the three methods were taken as input for the calculation of electron-optical phase images. The evolution of the real-space wave function of the electron beam in a TEM passing through the potentials was calculated using the multislice method [3] implemented within the Dr. Probe software package [30]. In this method, the sample is divided into a number of slices along the direction of the incident electron beam (the z direction). In the present calculations, the number of slices was chosen to be equal to the z sampling in the DFT simulations, and, hence, the potentials of the individual atoms were subsliced.

The following discussion is limited to the cases of monolayer and bilayer WSe_2, in which the effect of sample tilt on the measured average electron phase is negligible and where dynamic scattering effects play only a small role [11]. In addition to an incident electron energy of 80 keV, the parameters applied to the simulations included the aperture size, the sample tilt, the Debye-Waller parameters for the treatment of damping effects due to thermal atomic vibrations, as well as parameters for a quasicoherent image wave convolution in order to take into account image vibrations and sample drift accumulated over the long hologram exposure time of 12 s. For the Debye-Waller parameter, a single value was used for the Se and W atoms, which was the average of Debye-Waller parameters for the two elements measured by x-ray diffraction [31]. The simulation of monolayer WSe_2 was performed for an untilted sample and the parameters for the quasicoherent image wave convolution were chosen according to typical experimental values. In the case of bilayer WSe_2, the experimental parameters such as the sample tilt and the quasicoherent image wave convolution were determined by applying a Nelder-Mead minimization [32] of the root-mean-square differences between experiment and simulation for the 13 strongest beam amplitudes in the Fourier transform of the image wave function using the DFT electrostatic potential. Subsequently, the parameters for the correction of residual aberrations in the experimental phase were determined with the same algorithm minimizing the root-mean-square difference between the experimental and simulated real-space phase distribution of the image wave function. The experimental beam amplitudes were taken from a clean and almost defect-free area of the wave function presented in Ref. [11] that included 15 orthorhombic unit cells (see Supplemental Material [23]). The empirically chosen parameters for the simulation of the WSe_2 monolayer, as well as the optimized parameters for the simulation of the WSe_2 bilayer and the correction of the residual aberrations in the experimental bilayer phase image, are listed in the Supplemental Material together with an overview of the agreement achieved between the

TABLE I. Spatially averaged electron phase shifts for WSe_2 monolayer and bilayer structures obtained using the three different methods. Experimental values are taken from wave functions presented in Ref. [11].

	Monolayer (mrad)	Bilayer (mrad)
DFT	127.2	245.2
IDFT	134.5	258.5
IAA	138.4	267.1
Expt.	126 ± 5[a]	236 ± 10

[a] The experimental spatially averaged phase for a monolayer is determined from an extrapolation of values acquired for thicker structures and several samples.

experimental and simulated phase images for bilayer WSe_2 [23]. It should be noted here that a parameter optimization yielded identical parameters for the sample tilt and the quasicoherent image wave convolution when the phase image simulated using the IAA electrostatic potential was considered in the optimization instead of the phase image obtained with the DFT method. Consequently, the results are not affected by the choice of method considered in the parameter optimization.

Spatially averaged phases obtained from the multislice calculations are listed alongside our experimental results in Table I. It should be noted that aberration correction has no influence on the averaged electron phases presented here. Corresponding simulated phase images for a WSe_2 bilayer are shown alongside a cell average of the experimental phase image in Fig. 4.

For both monolayer and bilayer WSe_2, Table I shows that the DFT method yields the lowest average phase, while the IAA and IDFT results exceed the value obtained by the DFT method by approximately 9% and 6%, respectively. Remarkably good agreement is obtained between the average phase shifts obtained using the DFT-based simulations and the experimental values. For the WSe_2 monolayer, the spatially averaged phase obtained using the DFT method lies within the 1σ confidence interval for the extrapolated experimental value. For the WSe_2 bilayer the discrepancy is larger but still within the 1σ confidence interval. In contrast, the values obtained from the IDFT and IAA methods deviate significantly more from the experimental values.

The experimental and calculated phase distributions in Fig. 4(a) show a good match. The notable elliptical distortion at the positions of the atomic cores can be attributed to anisotropic image shift fluctuations resulting from sample vibrations, drift, or electrical instabilities of the lenses during the hologram exposure time of 12 s. From Fig. 4(b), it is apparent that the differences between the experimental and simulated phase images are mainly due to an offset in phase, which is smallest for the DFT method. The features in the difference phase images, such as those visible at $(x, y) = [(a/2), (\sqrt{3}/2)a]$, do not arise from systematic errors in the computed electrostatic potentials, as they do not follow the symmetry of the crystal. They are

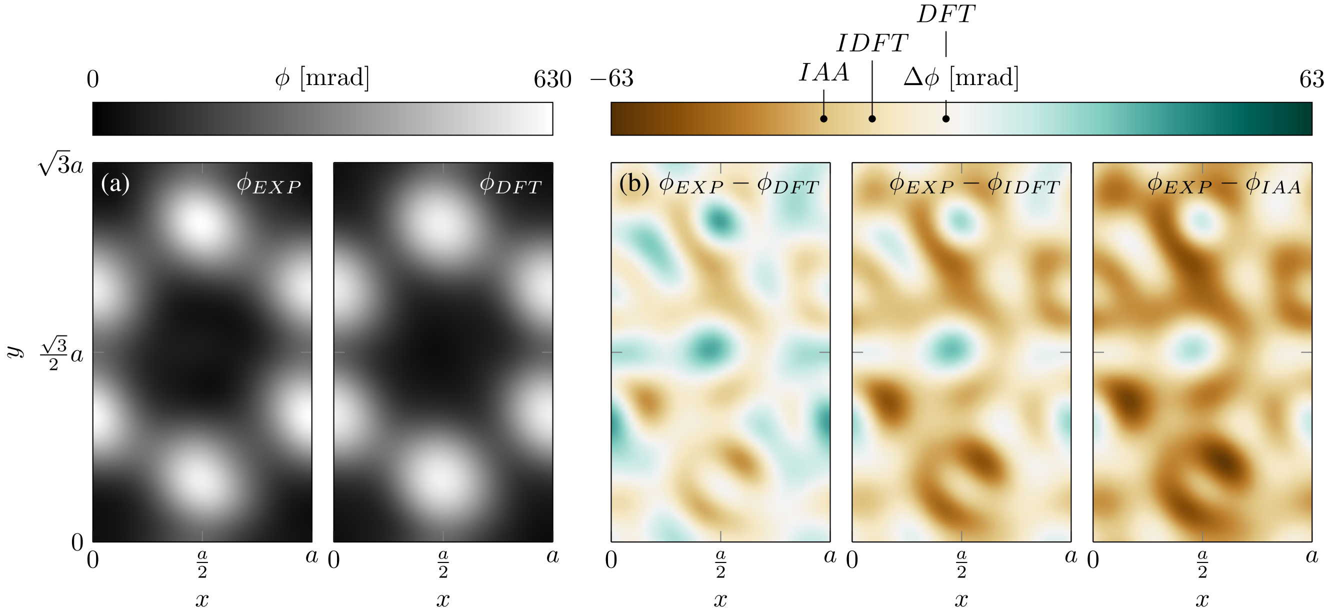

FIG. 4. Comparison between simulated and experimental phase images of a WSe_2 bilayer structure, shown for a region corresponding to the area marked by a blue rectangle in Fig. 1. Panel (a) shows an averaged experimental phase image of a WSe_2 bilayer [11], alongside a calculated phase image obtained with the DFT method. Panel (b) shows differences between phase images obtained with the three different methods and the experimental phase image. Positive values correspond to higher phases in the experimental phase image. The markings on the color bar represent the average difference for each method.

instead likely to be perturbations in the experimental data, the origin of which is the focus of ongoing studies. The residual fluctuations in the difference phase images of approximately 13 mrad are comparable to the vacuum phase noise of approximately 10 mrad, while a comparison between the phase images obtained with the DFT and IDFT methods (see Supplemental Material [23]) suggests that a noise level below 3 mrad would be necessary in order to resolve the spatial signature of bonding. The results, hence, indicate that, although the change in spatial electron density resulting from the effects of bonding and the associated change in electrostatic potential are nonhomogeneous effects and are only likely to be measurable when phase images with much better signal-to-noise ratios are available experimentally, the dominant effect of bonding on the measured mean electron phase is accessible from the present results.

We also studied interlayer coupling in the DFT model, which does not include van der Waals forces and, hence, only accounts for covalent effects. For this purpose, DFT and independent layer DFT results for a WSe_2 bilayer were compared. In independent layer DFT, the electrostatic potentials of the two layers forming a bilayer were calculated individually and then superimposed. The combined electrostatic potential was then used as input for a further multislice simulation, yielding an average electron phase shift of 245.3 mrad, which differs by only 0.04% from the DFT value for a WSe_2 bilayer (Table I). Since the main contribution in the interlayer coupling of two-dimensional materials is given by van der Waals forces, this small effect of covalent interlayer coupling is reassuring. Consequently, it is not expected that the electron beam will be sensitive to a shift in charge generated by covalent interlayer coupling. In order to estimate the effect of structural changes induced by van der Waals forces, which are expected to modify the interlayer distance w, we recalculated the average electron phase in the DFT method for a bilayer with a decreased interlayer distance. In our calculations, decreasing w for a WSe_2 bilayer by 6% (0.2 Å) led to a decrease of the average electron phase shift by only 0.03%, confirming the weak effect of interlayer coupling.

In conclusion, the electrostatic potentials of few-layer WSe_2 structures have been calculated using progressively more accurate methods and used as input for multisclice simulations of electron-optical phase images, for comparison with experimental results measured using off-axis electron holography. Our results demonstrate that a perfect contrast match can be achieved between experimental and simulated atomic-resolution phase images for a sample of precisely know thickness. Excellent agreement between simulated and experimental spatially averaged phase shifts is obtained when the effects of atomic bonding are taken into account in the simulations. If bonding effects are neglected, then the average phase can be overestimated in the simulations by up to 9% for a WSe_2 monolayer. This overestimate of the electron phase results from a change in electrostatic potential associated with a small redistribution in electron density along the bonding directions between the crystal atoms. This conclusion was confirmed by comparing theoretical and experimental results.

We employed a fast and accurate combination of DFT calculations using pseudopotentials and all-electron atomic corrections to restore core charge densities. Because of the low computational cost of this approach, it should allow quantitative analyses of defects and substitutional atoms in TMDs and other materials when large supercells are required, similar to high-resolution transmission electron microscopy studies on nitrogen substitutions in graphene [33].

The authors gratefully acknowledge computing time granted by the John von Neumann Institute for Computing (NIC) and provided on the supercomputer JURECA in the Jülich Supercomputing Centre (JSC) (JARA-HPC projects JIAS16 and JPGI90). Z. Z. acknowledges financial support from the European Commission under the Marie-Curie Fellowship (PIEF-Ga-2011-300036) and by Deutsche Forschungsgemeinschaft (DFG, German Research Foundation) Grant No. ZA 780/3-1. M. J. V. acknowledges a PDR grant from the Belgian Fonds National pour la Recherche Scientifique (GA T.1077.15) and ARC grand AIMED 15/19-09. J. B. acknowledges funding from German Science Foundation (DFG) Grant No. MA 1280/40-1. R. E. D.-B. acknowledges funding from the European Research Council (ERC) under the European Union's Seventh Framework Programme (FP7/2007-2013)/ERC Grant Agreement No. 320832.

---

[*] s.borghardt@fz-juelich.de

[1] R. E. Dunin-Borkowski, M. R. McCartney, and D. J. Smith, in *Encyclopedia of Nanoscience and Nanotechnology*, edited by H. S. Nalwa (American Scientific Publishers, Stevenson Ranch, CA, 2004), Vol. 3, pp. 41–99.

[2] P. A. Midgely and R. E. Dunin-Borkowski, Nat. Mater., **8**, 271 (2009).

[3] J. M. Cowley and A. F. Moodie, Acta Crystallogr. **10**, 609 (1957).

[4] E. J. Kirkland, *Advanced Computing in Electron Microscopy* (Plenum, New York, 1998).

[5] P. Kruse, A. Rosenauer, and D. Gerthsen, Ultramicroscopy **96**, 11 (2003).

[6] M. Y. Kim, J. M. Zuo, and J. C. H. Spence, Phys. Status Solidi A **166**, 445 (1998).

[7] P. Kruse, M. Schowalter, D. Lamoen, A. Rosenauer, and D. Gerthsen, Ultramicroscopy **106**, 105 (2006).

[8] M. Pierre, R. Wacquez, X. Jehl, M. Sanquer, M. Vinet, and O. Cueto, Nat. Nanotechnol. **5**, 133 (2010).

[9] J. Cai, F. Jelezko, and M. B. Plenio, Nat. Commun. **5**, 4065 (2014).

[10] R. S. Pennington, C. B. Boothroyd, and R. E. Dunin-Borkowski, Ultramicroscopy **159**, 34 (2015).

[11] F. Winkler, A. H. Tavabi, J. Barthel, M. Duchamp, E. Yucelen, S. Borghardt, B. E. Kardynal, and R. E. Dunin-Borkowski, Ultramicroscopy, DOI: 10.1016/j.ultramic.2016.07.016 (2016).

[12] B. Radisavljevic, A. Radenovic, J. Brivio, V. Giacometti, and A. Kis, Nat. Nanotechnol. **6**, 147 (2011).

[13] J. S. Ross *et al.*, Nat. Nanotechnol. **9**, 268. (2014).

[14] O. Lopez-Sanchez, D. Lembke, M. Kayci, A. Radenovic, and A. Kis, Nat. Nanotechnol. **8**, 497 (2013).

[15] C. H. Lee *et al.*, Nat. Nanotechnol. **9**, 676 (2014).

[16] Y. Gong *et al.*, Nat. Mater. **13**, 1135 (2014).

[17] M. Mahjouri-Samani *et al.*, Nat. Commun. **6**, 7749 (2015).

[18] A. Srivastava, M. Sidler, A. V. Allain, D. S. Lembke, A. Kis, and A. Imamoglu, Nat. Nanotechnol. **10**, 491 (2015).

[19] Y. M. He *et al.*, Nat. Nanotechnol. **10**, 497 (2015).

[20] X. Gonze *et al.*, Comput. Phys. Commun. **180**, 2582 (2009).

[21] X. Gonze *et al.*, Z. Kristallogr. **220**, 558 (2005).

[22] http://elk.sourceforge.net.

[23] See Supplemental Material at http://link.aps.org/supplemental/10.1103/PhysRevLett.118.086101, which includes Refs. [24–26], for a detailed description of the density functional theory calculation and the analysis of the experimental data.

[24] J. P. Perdew and A. Zunger, Phys. Rev. B **23**, 5048 (1981).

[25] D. R. Hamann, Phys. Rev. B **88**, 085117 (2013).

[26] H. J. Monkhorst and J. D. Pack, Phys. Rev. B **13**, 5188 (1976).

[27] W. L. Wang and E. Kaxiras, Phys. Rev. B **87**, 085103 (2013).

[28] A. Weickenmeier and H. Kohl, Acta Crystallogr. Sect. A **47**, 590 (1991).

[29] Here we approximate the mean inner potential of bulk WSe_2 with the average electrostatic potential of the central layer in the WSe_2 pentalayer structure.

[30] J. Barthel, http://er-c.org/barthel/drprobe.

[31] F. Z. Chien, Y. S. Chen, Y. C. Chu, W. Y. You, J. B. Lee, T. E. Dann, C. H. Tu, and Y. S. Huang, Chin. J. Phys. **26**, 119 (1988).

[32] J. A. Nelder and R. Mead, Computer Journal (UK) **7**, 308 (1965).

[33] J. C. Meyer *et al.*, Nat. Mater. **10**, 209 (2011).